

Research Article

Investigation on Wheel-Rail Contact and Damage Behavior in a Flange Bearing Frog with Explicit Finite Element Method

Yuan Gao ^{1,2}, Ping Wang ^{1,2}, Yibin Liu,^{1,2} Jingmang Xu ^{1,2}, Zhiguo Dong,^{1,2}
and Kai Wang^{1,2}

¹MOE Key Laboratory of High-Speed Railway Engineering, Southwest Jiaotong University, Chengdu 610031, China

²School of Civil Engineering, Southwest Jiaotong University, Chengdu 610031, China

Correspondence should be addressed to Jingmang Xu; mang080887@163.com

Received 15 July 2019; Revised 30 September 2019; Accepted 20 November 2019; Published 14 December 2019

Academic Editor: Paolo Lonetti

Copyright © 2019 Yuan Gao et al. This is an open access article distributed under the Creative Commons Attribution License, which permits unrestricted use, distribution, and reproduction in any medium, provided the original work is properly cited.

Flange bearing frogs are designed to provide continuous rolling surfaces for trains traveling on the through line, but the interaction between wheel and rail in a diverging line is more complex than that for a common crossing, especially including flange bearing mode and multipoint contact during the transition. The wheel load will be transited from tread to flange and back to tread, which will intensify the wheel-rail interaction. In this paper, a numerical procedure is presented for the analysis of wheel-rail rolling contact behavior and damage prediction for the flange bearing frog. The three-dimensional explicit finite element (FE) model of a wheel passing the flange bearing frog is established to obtain the dynamic wheel-rail interaction in both the facing and the trailing move. The evolution of contact forces, the distribution of adhesion-slip regions, and shear surface stress and microslip at the contact patch are revealed. Then, the competition relationship between RCF (rolling contact fatigue) and wear of a flange bearing frog is analyzed. The results of numerical simulations can contribute to an understanding of the mechanism of the transient rolling contact behavior and provide guidance in design optimization for flange bearing frogs.

1. Introduction

Turnouts are essential components of railway infrastructure, providing flexibility in traffic operation. To enable a vehicle to change between tracks, the profiles of switch and frog rail are designed to vary in turnout. The variation of rail profiles will change the wheel-rail contact parameters, and the combination of point rail and wing rail carrying the wheel loads together leads to more complicated multipoint contact in railway turnouts [1, 2]. The normal wheel-rail contact relationship is altered when wheel load is transferred from the point rail to the wing rail in the crossing panel, sometimes resulting in severe impact between wheel and rail. Due to the lateral displacement of wheelsets and the varied rail profiles, dynamic vehicle-turnout interaction is a time variant process and is a far more complex process than passing along ordinary tracks. These factors will ultimately lead to serious damage to the components of railway turnout and result in the transmission of noise and vibrations to the

external environment. Railway turnouts have therefore become a key part of the railway infrastructure which limits vehicle speeds [3, 4]. However, most turnouts on heavy haul railways and existing lines are subject to straight track passing. For some railway turnouts at catch sidings and arrival-departure tracks, the number of diverging passing vehicles can be less than 1% of the number of straight passing vehicles. During the passage of wheels over the railway turnout, the structural irregularity and the gap in conventional fixed frog will significantly affect the running behavior of railway vehicles in terms of stability, passenger comfort, and derailment prevention.

In order to reduce the dynamic wheel-rail impact between wheels and turnout rails, flange bearing frogs can be applied to prolong turnout service life while satisfying the operational requirements of the railway. The structure of a flange bearing frog is shown in Figure 1, and the frog consists of the flange bearing part, the mainline rail, and the tread bearing part, which is highlighted in green, red, and yellow,

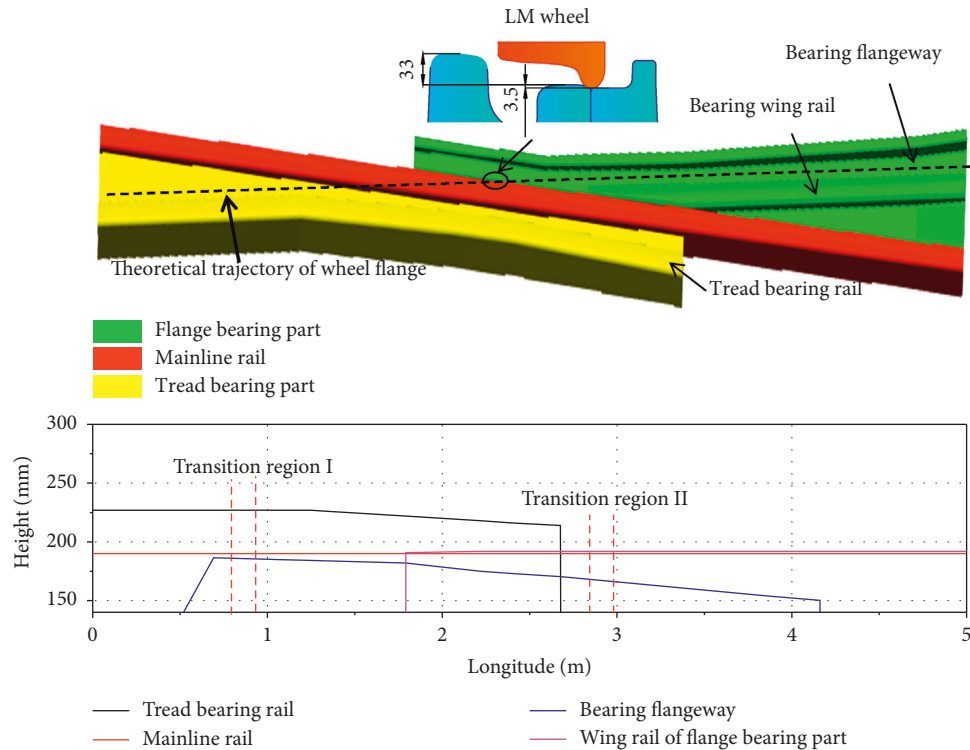


FIGURE 1: Rail height along longitudinal direction of frog.

respectively (Figure 1). The mainline rail is installed between the tread bearing part and the flange bearing part, and the three components are connected with horizontal bolts. As shown in Figure 2, the facing point ramp is the tread bearing of the frog, while the trailing point is the flange bearing. The mainline rail is a continuous structure in through direction, and its geometric profile along longitudinal direction is not subject to dynamic evolution in space; the dynamic wheel-rail response during the passage of wheels over the turnout in through direction will be the same as that for open tracks. The flange bearing frog can provide continuous rolling surfaces for the wheels in the through direction, but the wheel-rail interaction in the diverging line is more complicated than that for a common crossing. When the train passes the flange bearing frog in divergent direction, the wheel load will be transferred from the tread to the flange and back to tread, coupled with the influence of structural irregularity of the flange bearing frog. In addition, though the rail opposite the frog has a ramp that matches the frog in the design to equalize the wheel load, the dynamic response in divergent direction between wheel and flange bearing frog is still violent. As the weak link of the flange bearing frog in actual service conditions, it is of great significance to investigate the wheel-rail contact behavior and related degradation of frog rails when trains pass in the diverging direction.

The wheel-rail dynamic contact relationship in turnout is very complicated. One way of analyzing this is the FE method. Andersson and Dahlberg [5] established the frog beam model based on the finite element method, and the wheel-rail impact response caused by frog gaps through

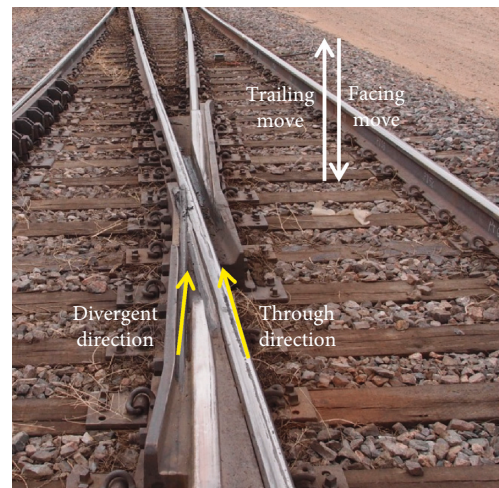


FIGURE 2: Structure of flange bearing frog.

virtual beam elements is obtained; however, this model is only suitable for the simulation of vertical vehicle-turnout coupling dynamics. Kassa and Nielsen [6] put forward a finite element model that considered the flexible characteristics of the turnout system, and the wheel-rail interaction at the turnout areas using DIFF3D is calculated according to the practical model. Alfi and Bruni [7] presented a dynamic vehicle-turnout coupling model that took into account the influence of multipoint contacts and elastic tracks under the dynamic medium frequency (MF) response of 0–500 Hz, and then the influence of wheel-rail wear and track irregularity on the dynamic wheel-rail interaction in turnouts is

investigated. Ren et al. [8] calculated the wheel-rail force transfer/distribution characteristics of turnout areas based on the vehicle-turnout space coupling vibration model, and then a method for reducing dynamic wheel-rail response through optimization of the sectional geometric profile of frog crossing is introduced. Johansson et al. [9] predicted the plastic deformation of rails using a local 3D wheel-rail contact model based on the dynamic wheel-rail response obtained using GENSYS, and the growth of the turnout rolling contact fatigue based on the rail surface fatigue indices is also presented. Rocha [10, 11] assessed the running safety of high-speed trains on a short-span bridge combined with the Monte Carlo method and extreme value theory, and then the comparison between the results of European standards approach and probabilistic approach is evaluated, obtaining the safety assessment results and precise maximum allowable speed. The frictional rolling contact and structural vibration between wheel and rail are usually solved independently by the quasistatic or MBD methods, which cannot consider the influence of the dynamic wheel-rail interaction on the evolution of frictional contact, such as the wave propagation, and the accurate contact solutions cannot be obtained. In addition, the variable profile along the frog will result in the change of contact parameters, and the interaction between the wheel and frog is more complicated due to the variable contact geometry relationship in the turnout frog. In order to investigate the interaction between wheel and frog rail, the implicit-explicit integration method is applied to simulate the problem of high-speed impact and transient contact, which is the widely accepted approach to simulate the impact in frog, and the explicit finite element method is thus selected as the appropriate way to solve the interaction between wheel and rail. Wiest et al. [12] established a simplified finite element model for elastoplastic wheel-rail contact frogs based on Abaqus and presented the change of stress-strain fields at crossing when wheels passed through the frog several times; however, the evolution characteristics of the geometric profile of frog sections along spaces were not taken into account. Greco et al. and Lonetti et al. [13, 14] put forward a numerical strategy based on a moving mesh technique to simulate the vehicle-bridge interaction in railway bridges and then evaluated the influence of coupling effects between bridge deformations and moving loads considering the neglected nonstandard terms in the inertial forces concerning both centripetal acceleration and Coriolis acceleration, providing an advanced numerical modeling approach. Davis et al. [15] put forward a finite element model for single-wheel-impact turnouts considering the accumulated plastic strain under cyclic wheel loads and the variable adaptability of profile spaces, and then a contrast analysis on the influence of three kinds of frog materials on the growth of cracks based on the obtained wheel-rail contact/shear/residual stresses and a two-dimensional (2D) crack model was performed. Pletz et al. [16, 17] presented a dynamic finite element model for wheels passing through frog and obtained the dynamic wheel-frog contact force and vertical wheel displacement as well as the angular velocity of the wheels, the generation of the stress field, and the plastic deformation of frogs. Guo

et al. [18] evaluated the wheel-rail contact behavior at frogs based on the explicit integral algorithm at different speeds, including the stress, plastic strain, and damage characteristics at frog crossings when the materials were subject to nonlinear work hardening. Xin et al. [19] calculated the stress/strain distribution from fixed frogs based on explicit rolling contact model. Then, the angles of frog nose rail cracks and the predicted residual life based on the J-S fatigue criterion were calculated; the obtained results coincided well with those observed on-site. Wei et al. [20, 21] established a three-dimensional (3D) wheel-rail rolling contact model for frog using commercial LS-DYNA software, and then a precise analysis for the rolling contact solution of frog is paid particular attention to, especially the tangential results, the adhesion-slip distribution in contact patches, and microslip at two-point contact, and then the authors presented a performance evaluation method for fixed frogs in long-term service based on the FE model, obtaining the frog profile and rail stiffness under actual operating conditions. Ma et al. [22] analyzed the dynamic impact effect at frog crossing based on a combination of field experiment and the explicit finite element method, thus obtaining the adhesion-slip distribution and contact stress distribution during the passage of wheel over the turnout, and then the accuracy of finite element method using self-adaptive mesh refinement is verified. Combined with experimental validation and simulation results, the explicit finite element method is widely applied, and more detailed analyses have been carried out, including those looking into wheel/rail high frequency vibrations and the profile evolution of wheel and rail in turnout. Thus far, the explicit finite element method can be used to simulate the transient wheel-rail rolling contact behavior of turnout areas considering real contact geometry and nonlinear materials. However, similar research findings are mainly aimed at fixed frogs in heavy haul turnouts or movable frogs in high-speed turnouts. Few studies have been presented to investigate the interaction between flange bearing frog rail and wheel; besides, the accurate contact stress is hard to measure due to the complex fission structure, so the explicit FE method can be adopted to investigate the wheel-rail contact behavior and the evolution of contact stress.

In this paper, the wheel-rail contact behavior of a wheel passing a flange bearing frog is simulated, using the explicit finite element model based on the central difference method. Then, the transient contact solutions, such as dynamic contact force, adhesion-slip regions, surface shear stress, and microslip, are obtained. Furthermore, the competition between wear and RCF at different regions in flange bearing frog is evaluated based on the damage coefficient functions of wear numbers. The results of the study can provide a theoretical basis for optimization, damage control, and maintenance of flange bearing frog.

2. Modeling of a Flange Bearing Frog

In this paper, a 12# turnout of the flange bearing frog is selected as the research target with the nominal profile of 75 kg/m rail, which are processed with online heat treatment. A schematic diagram of the model is shown in Figure 3.

To investigate the dynamic wheel-rail interaction in a flange bearing frog, a 3D geometric model for wheel-rail contact in flange bearing frogs is established using hybrid scanning instructions. The length of the frog model is 15.992 m to eliminate the influence of boundary effect [23]. The profile of wheel and rail is LM and CHN70, respectively; to ensure the real contact shapes in potential contact regions, the self-adaptive mesh refinement method is adopted in the model. The geometric profiles of the typical frog sections are obtained based on the linear interpolation method (one typical section per 0.1 m); the relative position and spatial coordinates of the wheel and rail are ensured according to the geometric constraint conditions for wheel-rail contact in frog. The frog is assembled in strict accordance with the feature sizes and relevant standards. Next, the assembled 3D geometric model will be imported into Hypermesh and discretized by transitional 8-node solid elements to embody the flexibility characteristics of the wheel and flange bearing frog rail. The rail pad can be simulated by linear springs and viscous dampers, and the stiffness and damping can be obtained from the actual operational conditions at a heavy haul line, with the corresponding values of 90 mN/m and 75 kN·s/m [24]. The 3D explicit finite element model includes about 212.3w elements (Figure 3). Based on the geometry features of the wheel and flange bearing frog, the self-adaptive mesh refinement method is applied in the model; the size of the elements in a potential contact zone should be less than 1 mm, while the maximum size of elements in noncontact regions can reach up to 20 mm, in order to ensure the accuracy and reliability of the calculated results. The wheel-rail contact can be simulated through the surface-to-surface contact algorithm based on the penalty function. The rubber pad modeled by linear springs and viscous dampers is installed at the bottom of the flange bearing frog, which is simulated by a uniform grid of 7×7 discretely distributed spring-damper pairs. As for the horizontal constrained condition, the connecting function of bolts between the three parts can be simulated as discrete beam elements. All parts above the vehicle-suspension system are simplified as lumped mass which are connected with the wheel axle through the primary suspension modeled by linear springs and viscous dampers; the stiffness and damping of the primary suspension are 17 mN/m and 3 kN·s/m, respectively. Considering the actual service conditions of frog, the profile of a worn LM wheel is used in the model (Figure 4); the profile of the wheel is measured on the heavy haul railway using a wheel-rail profile tester MiniProf. The measurement accuracy can reach up to 0.01 mm.

In order to precisely determine the running direction of the wheel, an Oxyz 3D Cartesian coordinate system is established to define the motion direction. The coordinate origin is set at the initial position near the throat at the tread bearing part. The x - and z -axes refer to the longitudinal direction (theoretical trajectory of the wheel) and the lateral directions, respectively, and then the kinematic and dynamic results in the explicit analysis are calculated in the global coordinate system; the Matlab program was developed for the coordinate transformation of contact solutions, including the distribution of adhesion-slip

regions, surface shear traction, and microslip, and then the contact solutions are applied to calculate the stress and wear index distribution during the passage of wheel. The bilinear elastoplastic material is applied in the model of flange bearing frog with the yield stress equaling 800 MPa. According to the vehicle space model parameters of C80 train [24], the detailed parameters of the explicit finite element model are shown in Table 1.

The contact solutions can be calculated through a combination of a static analysis using an implicit integration method and a dynamic analysis using an explicit integration method. The displacement field of the wheel-rail system under a static wheel load is calculated in the implicit integration method, which is then treated as the initial state of the dynamic model when stress initialization is performed. This step is necessary to avoid the unrealistic vibration that may be induced by in-equilibrium state of the system. Meanwhile, the translational and angular velocities applied on the wheel are taken as the initial conditions, and a certain torque is exerted on the wheel axle to simulate the traction/brake effects.

During the passage of wheel over the flange bearing frog, most of the nodes in the FE model are in multiaxial stress conditions, and stress components in the model must be taken into account simultaneously. In order to qualitatively describe the variation rule of the plastic deformation during transition, the comparison between von Mises stress and yield strength can be applied to qualitatively describe the distribution of plastic deformation, which can be used as an index to evaluate the degradation of frog rail. The calculation formula of von Mises is shown as follows:

$$\sigma_e = \sqrt{\frac{1}{2} [(\sigma_1 - \sigma_2)^2 + (\sigma_2 - \sigma_3)^2 + (\sigma_1 - \sigma_3)^2]}. \quad (1)$$

3. Verification of the Model

The contact force between wheel and rail cannot be measured accurately by the experimental method, and the solution of wheel-rail interaction is rarely verified directly especially in dynamic condition [25], so the indirect verification method is proposed.

Before the wheel enters the transition regions of frog, the wheel will remain in an approximately steady state, and the vertical force will be fluctuated around the wheel load slightly. The contact solution of such instants can be used to verify the feasibility of the explicit wheel-rail finite element model. The contact solution of the explicit FE method was verified at 0.5 m with CONTACT, and the results of contact force and stress agree well as shown in Figure 5 and Table 2; therefore, the model can precisely be applied to simulate the interaction between wheels and rail.

4. Evolution of Dynamic Wheel-Rail Force

The structural components and geometric profiles of the flange bearing frog are significantly different from those of the conventional fixed frog. Complicated wheel-load transitions and multipoint contact behavior will exist in the frog,

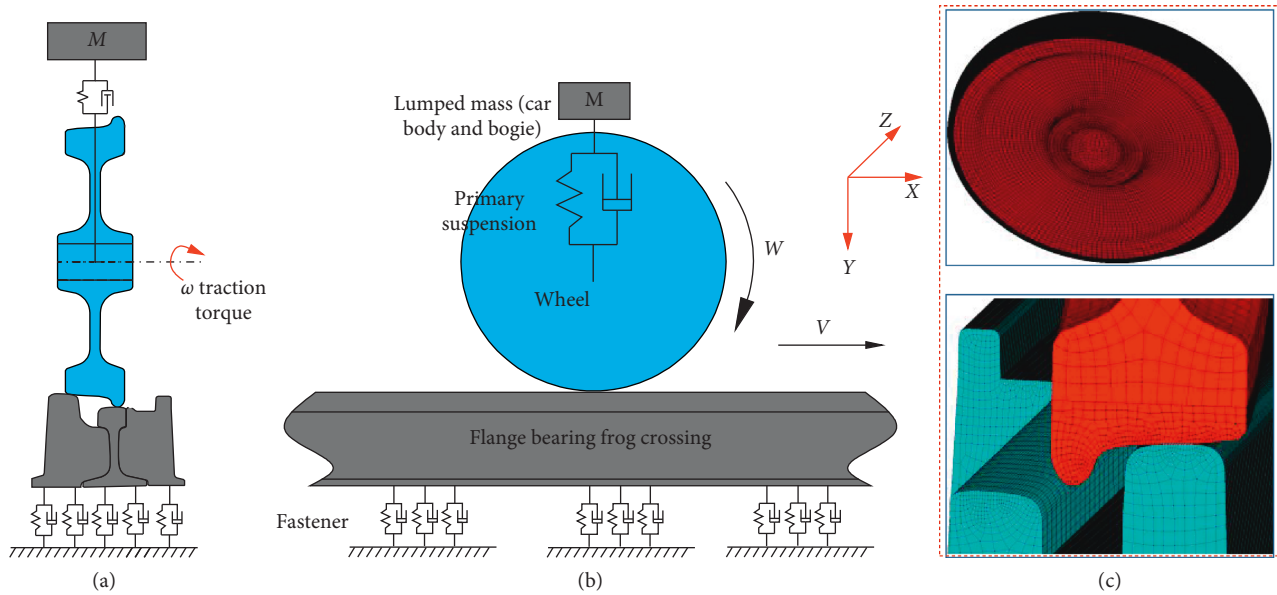


FIGURE 3: Schematic diagram of wheel-rail contact model in a flange bearing frog with close-up mesh: (a) the left view of the schematic diagram of the model; (b) the front view of the schematic diagram of the model; (c) the close-up mesh.

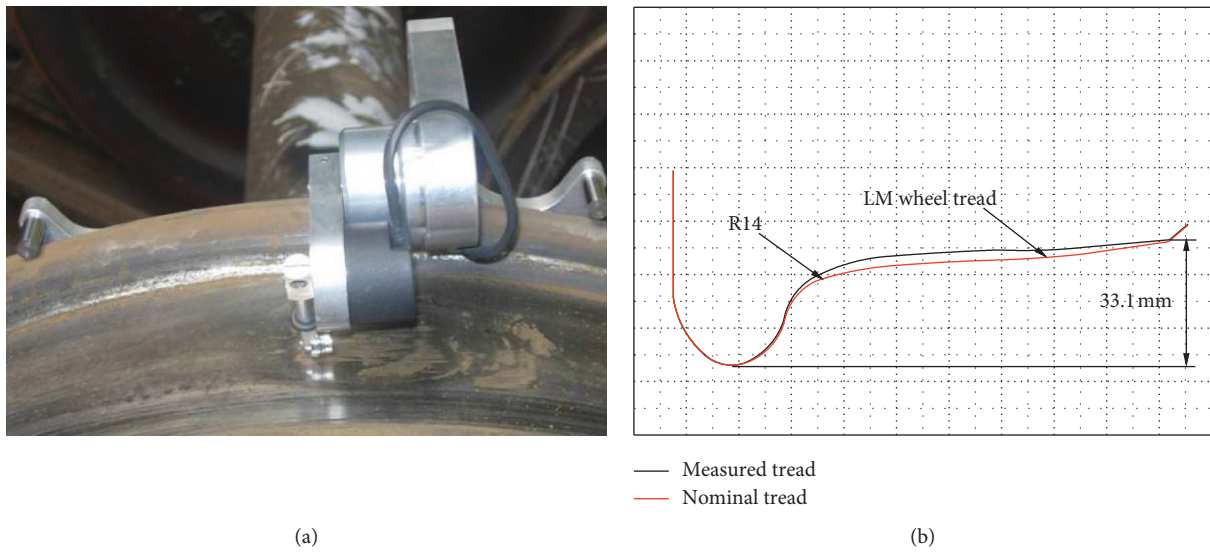


FIGURE 4: Comparison of measured and nominal wheel profile.

leading to significant changes in contact parameters during wheel-rail rolling contact. The wheel-rail contact forces are shown in Figure 6 when the wheel passes the frog in facing move/trailing move at a speed of 15 km/h.

For the condition of the wheel passing in facing movement in Figure 6(a), the initial wheel/rail contact point is set at the rail surface of the tread bearing part. During the passage of wheel over the frog, the trajectory of the running direction will deviate from the longitudinal axle of the tread bearing rail, causing the wheel-rail contact point to gradually move to the outside of the wheel tread. In the transition region of tread bearing part, the tread will contact with the tread bearing rail at first (Figure 7, S1), then the tread and flange will contact with tread bearing rail and mainline rail,

respectively, as the wheel continues to run (Figure 7, S2), and the load will be transferred from tread to flange when the wheel passes through the mainline rail of the frog (Figure 7, S3). The top bearing width of the mainline rail is narrow, meaning the wheel-rail contact force will not reach peak value within a short time, so the maximum wheel-rail contact force excited at the mainline rail will be lower. After the transition, the wheel will pass through the mainline rail and come into contact with the bearing flangeway. The height difference between mainline rail and bearing flangeway forms the irregularity of height; therefore, the wheel-rail dynamic interaction will be intensified at this time, and the maximum wheel-rail force can reach up to 181 kN. Due to the fact that the contact force in facing direction is larger

TABLE 1: Values of parameters used in the model.

	Parameter	Value
Primary suspension	Axle load (t)	25
	Stiffness coefficient ($\text{MN}\cdot\text{m}^{-1}$)	17
	Damping coefficient ($\text{kN}\cdot\text{s}\cdot\text{m}^{-1}$)	3
Wheel and rail materials	Elasticity modulus (GPa)	210
	Yield strength (MPa)	785
	Strain hardening modulus (GPa)	14.879
	Density ($\text{kg}\cdot\text{m}^{-3}$)	7800
	Tangential Young's modulus	20.6
	Poisson's ratio β	0.3
	Damping constant	0.0001
Rubber mat	Stiffness coefficient ($\text{MN}\cdot\text{m}^{-1}$)	90
	Damping coefficient ($\text{kN}\cdot\text{s}\cdot\text{m}^{-1}$)	75
	Elasticity modulus (GPa)	210
Contact parameters	Coefficient of friction	0.5

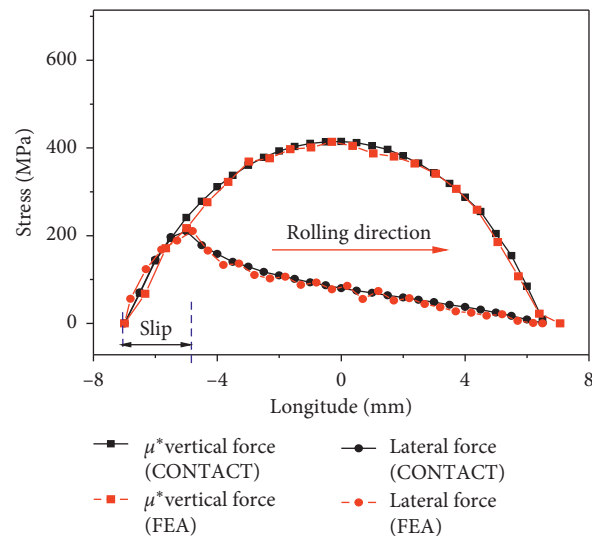


FIGURE 5: Verification of contact results.

TABLE 2: Comparison of results of different methods.

Approach	Contact patch			Maximum stress	
	Semiaxis (mm)	Semiaxis (mm)	Area (mm^2)	Vertical (MPa)	Shear (MPa)
CONTACT	7.36	5.65	130.6	832.1	224.1
FE method	7.42	5.45	127.0	846.3	236.4
Difference with respect to CONTACT (%)	-0.82	3.66	2.83	1.71	5.2

than the force in trailing direction, the latter simulation results are obtained from the condition in facing move.

When the wheel continues running along the bearing flangeway rail, the flange will solely bear the entire wheel load (Figure 7, S4), and the fluctuation amplitude of the wheel-rail force will gradually attenuate under the effect of damping from the fasteners and structure. In the end, the dynamic load will fluctuate around the half of static wheel load (122.5 kN). In the transition region at the flange bearing part, the flange will contact with bearing flangeway at first (Figure 7, S5); with

the height of bearing flangeway decreasing, the wheel load will be transformed from flange to tread (Figure 7, S6), the tread and flange will contact with bearing wing rail and bearing flangeway at the same time, and the wheel-rail interaction will be exacerbated under the influence of structural irregularities. After the transition, the wheel tread will solely bear the wheel load (Figure 7, S7), and the maximum value of the wheel-rail vertical contact force will reach up to 162 kN.

In order to analyze the evolution rules of the longitudinal force along the frog rails, the constant torque prescribed on

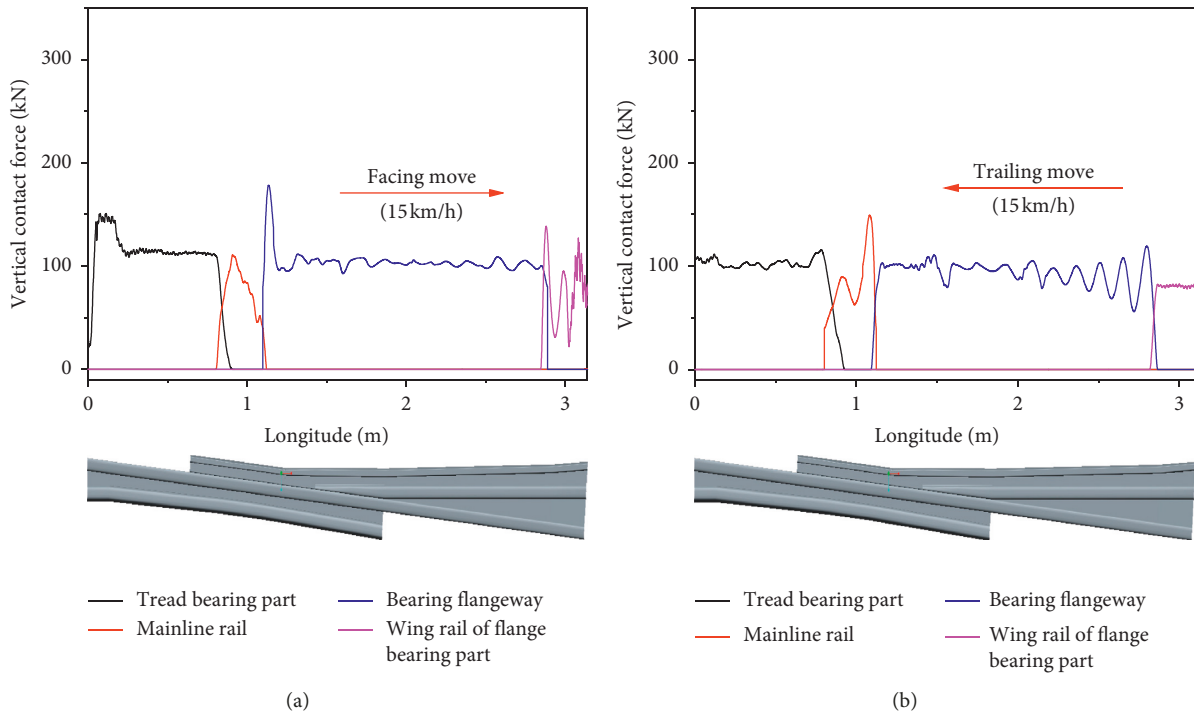


FIGURE 6: Evolution of vertical force with the wheel passing through (a) vertical force of trailing move and (b) vertical force of facing move.

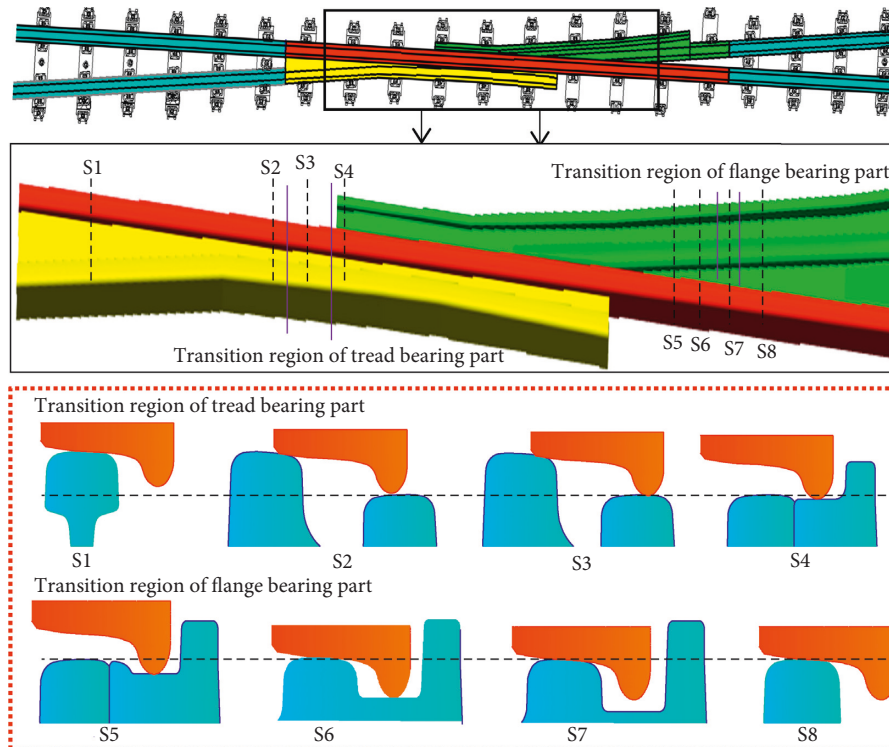


FIGURE 7: The contact behavior between wheel and rail during transition.

the axle of the wheel is assumed to generate a longitudinal traction force equal to 30% of the static axle load.

As shown in Figure 8, before the wheel enters into the transition regions of flange bearing frog, the wheel runs in

approximately steady state; therefore, the longitudinal force is equal to the product of vertical contact force and traction coefficient. The longitudinal contact force will increase under the effect of traction torque prescribed on the wheel

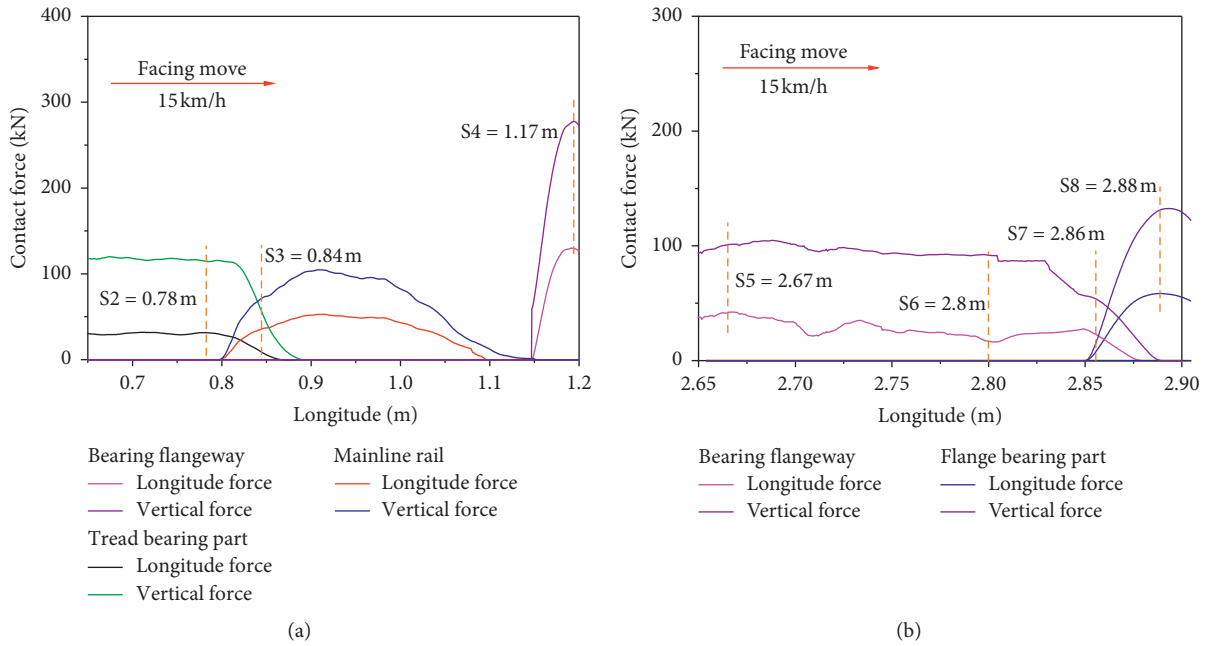


FIGURE 8: The evolution of longitudinal force in facing move (a) vertical and longitudinal forces at the transition region of the tread bearing part and (b) vertical and longitudinal forces at the transition region of the flange bearing part.

and impact induced by structural irregularities, which may change the adhesion-slip distribution in contact patch, and the slip regions in contact patch will increase (Figure 9), leading to more severe wear of frog rail. However, the ratio of longitudinal force and vertical force is always less than the frictional coefficient, and the longitudinal contact force decreases to zero within a very short time during the two-point contact status. During the transition, the ratio of the longitudinal force to normal force varies along the rail with time, and the variation can be exacerbated by the geometric irregularities of the frog. When the wheel enters the transition region at the flange bearing part, the wheel load will be transited from the flange to the wheel tread with a decrease in bearing flangeway height, leading to violent wheel-rail impact, the higher contact force will increase the stress, resulting in the faster wear development rate of the rail, and the maximum value of longitudinal force is equal to 85.4 kN.

According to Figures 8 and 10, eight typical instants are selected to investigate the evolution rule of frictional contact solutions during the transitions; S2~S4 are, respectively, 0.78 m, 0.84 m, and 1.17 m; among them, S1 represents the instant that the wheel is located at the rail before transition; S2 represents the instant with the contact between tread and tread bearing rail during transition; S3 represents the two-point contact status, where the tread and flange will be in contact with tread bearing rail and mainline rail at the same time; and S4 is the instant corresponding to the maximum contact force after transition, where the flange will solely bear the wheel load; S5~S8, are respectively, 2.67 m, 2.8 m, 2.86 m, and 2.88 m; among them, S5 is the instant when the wheel runs in approximately steady state with the contact between wheel and bearing flangeway after impact; S6 is the

instant corresponding to two-point contact status, where the tread and flange will be in contact with the bearing wing rail and bearing flangeway at the same time; S7 is the instant with maximum contact force after transition in flange bearing part; and S8 is the instant when the wheel passes through the frog. The typical instants mentioned above include the approximate steady state, two-point contact state, and impact state with maximum contact force, which can be beneficial for us to recognize the evolution of contact solutions at flange bearing frog.

Figure 10 shows the vertical displacement of wheel during transition; during the transition, the wheel load will be transformed from tread to flange, and the height of tread bearing rail will decrease (S1-S2) until the tread and flange are in contact with tread bearing rail and mainline rail simultaneously. Then, the wheel will move to the gage corner laterally on mainline rail; as a result, the height of wheel will continue to drop (S2-S3), and then the wheel will pass over the mainline rail into bearing flangeway; the height of wheel will drop quickly (S4) due to the effect of the height difference between bearing flangeway and mainline rail. When the contact patch is located at the transition regions of flange bearing part, the process of wheel-load transition is accomplished by the ramps of bearing flangeway, and the wheel drops with the height decrease of bearing flangeway (S5-S6); therefore, the tread and flange will be in contact with bearing wing rail and bearing flangeway (S6) simultaneously, and the wheel load will be transformed from flange to tread. After the transition, the height of the wheel will remain constant (S7-S8). It is worth noting that the dynamic response obtained from simulation is not affected by the other distractions, so there is no need to apply filtering methods to deal with signals.

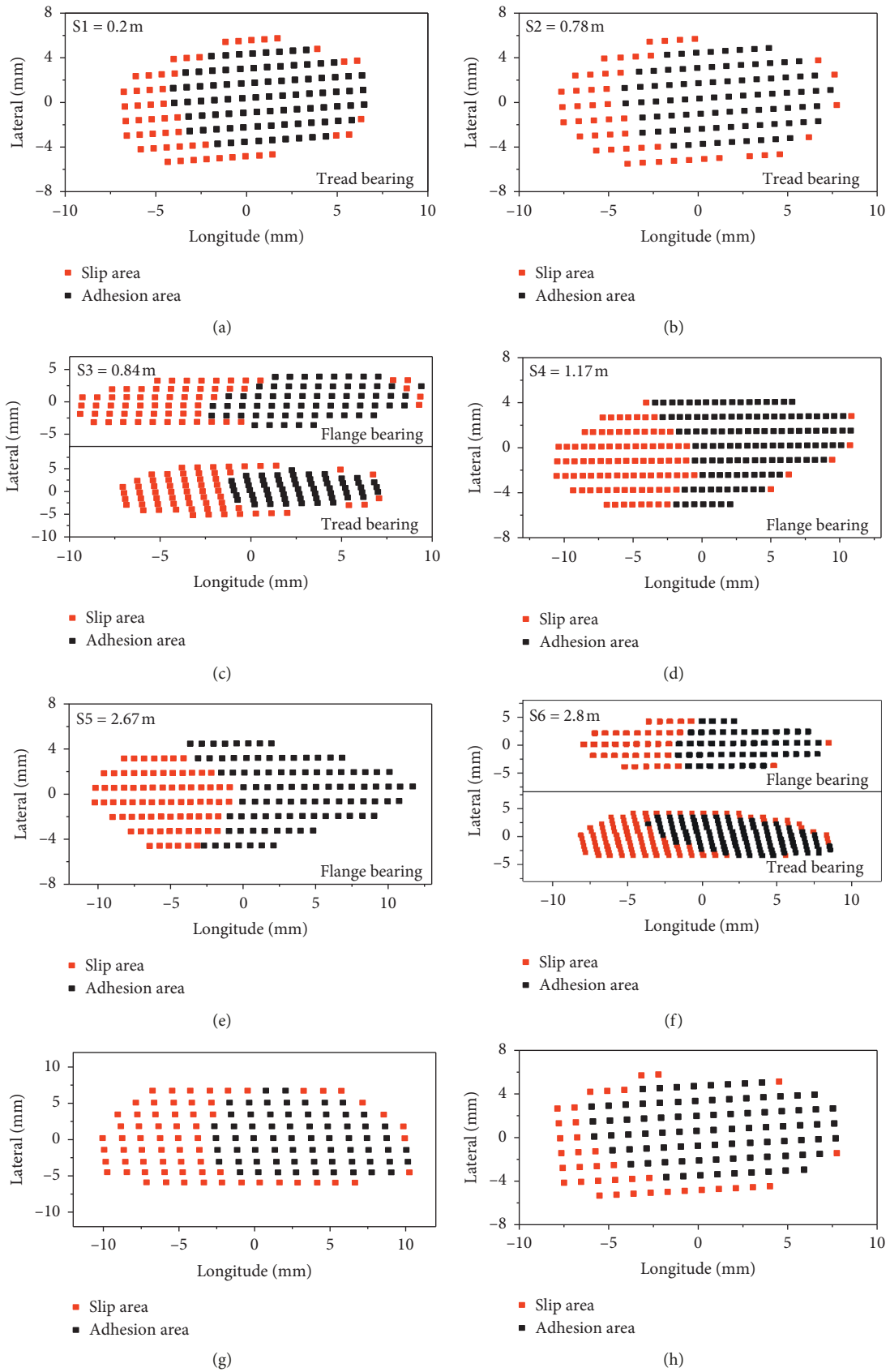


FIGURE 9: The distribution of the adhesion-slip region during transition in the tread bearing part and flange bearing part: (a) S1; (b) S2; (c) S3; (d) S4; (e) S5; (f) S6; (g) S7; (h) S8.

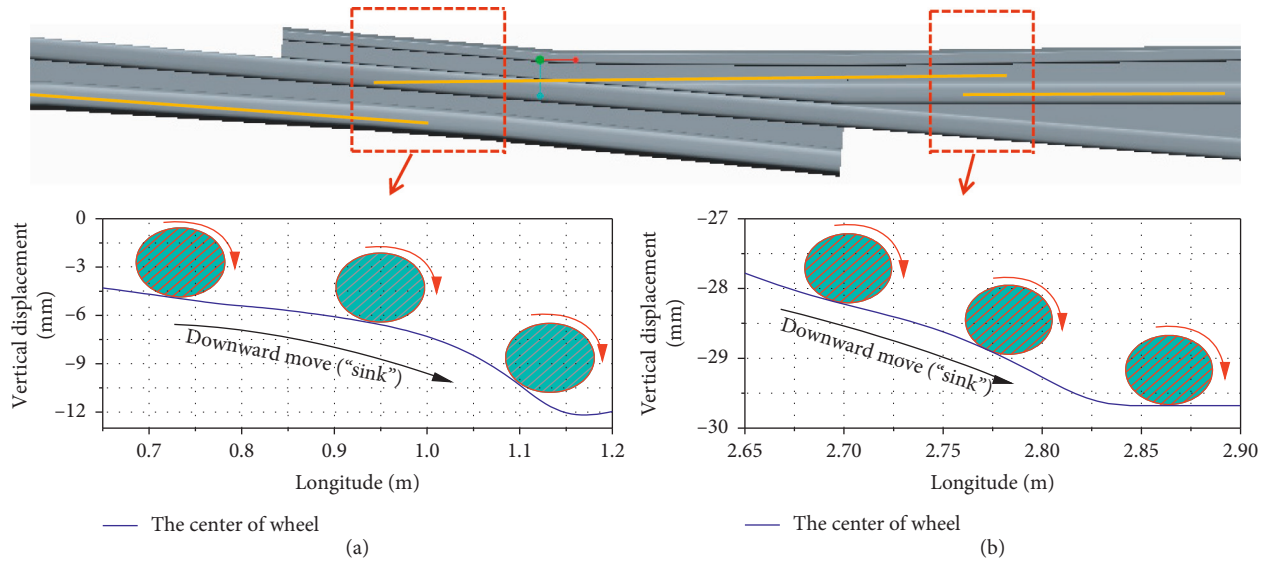


FIGURE 10: The vertical displacement of the wheel during transition: (a) the vertical displacement in tread bearing part and (b) the vertical displacement in flange bearing part.

5. Evolution of the Rolling Contact Solution

In this section, a detailed analysis of the wheel-rail rolling contact solution is conducted at different instants in the transition regions during the passage of the wheel over the frog at 15 km/h in facing move. The magnitude and distribution of contact solutions can be derived from the explicit finite element model, including the contact stress, slip, and microslip, which can be applied to indicate the frictional rolling contact behavior between wheel and rail in the frog.

5.1. Adhesion-Slip Region Distribution Characteristics in the Contact Zone. When the value of shear force is equal to the Coulomb friction threshold, due to the differences in deformation between the wheel-rail contact regions, there must be a region in the wheel-rail contact patch where the two contact surfaces are subject to relative slip, which form the slip region. An element in the contact patch will be in the slip region when the total tangential force of the element (x, y) is higher or equal to the maximum permitted sliding friction force; when the total tangential force of the element (x, y) is lower than the maximum permitted sliding friction force, the element will be in the adhesion region. See the following formula for the detailed expression:

$$\begin{cases} \sqrt{\sigma_x(x, y)^2 + \sigma_y(x, y)^2} \geq f\sigma_z(x, y), & \text{slip region,} \\ \sqrt{\sigma_x(x, y)^2 + \sigma_y(x, y)^2} < f\sigma_z(x, y), & \text{adhesion region,} \end{cases} \quad (2)$$

where $\sigma_x(x, y)$, $\sigma_y(x, y)$, and $\sigma_z(x, y)$ are the longitudinal, vertical, and lateral creep forces of the element (x, y) in the contact patch, with f being the frictional coefficient.

Figures 9(a)–9(d) show the distribution of adhesion-slip regions during transition in tread bearing part. The higher surface shear force will lead to larger area of slip region in the

wheel-rail contact patches. According to the area of slip regions shown above, under the effect of wheel-rail impact induced by frog structural irregularities, the adhesion coefficient between wheel and rail is decreased, which leads to larger slip regions as shown in Figures 9(d) and 9(f); when the wheel load is transformed from tread to flange, the area of the slip region in contact patch increases from 32% to 43% during transition, which may lead to quicker wear development rate.

Figures 9(e)–9(h) show the distribution of adhesion-slip regions in flange bearing part during transition. Compared with the tread bearing mode, the contact angle and size of contact patch are relatively smaller when the flange solely bears the wheel load, resulting in longer and narrower contact patch, and the area of the contact patch increases by 12.3% from S5 to S7, while the area of the slip region increases from 45.7% to 54.9%. Similarly, the effect of impact on the distribution of the adhesion-slip region is significant, and the growth rate of the slip region in the contact patch is higher compared to that in the tread bearing part during transition.

5.2. Distribution Characteristics of Surface Shear Traction in the Contact Zone. The traction/braking force acting on the wheel will intensify the tangential contact force on the rail surface. In order to describe the magnitude and distribution of the surface shear stress during transition, a detailed analysis of surface shear stress at eight instants will be performed.

Figure 11 shows the distribution of surface shear stress field during transition in tread bearing part. The vector of the surface shear stress in Figure 11(a) is consistent with the running direction of the wheel in general. However, the vector will deflect slightly since the running direction of the wheel does not coincide with the longitudinal axis of the tread bearing rail; Figure 11(b) shows the surface shear stress

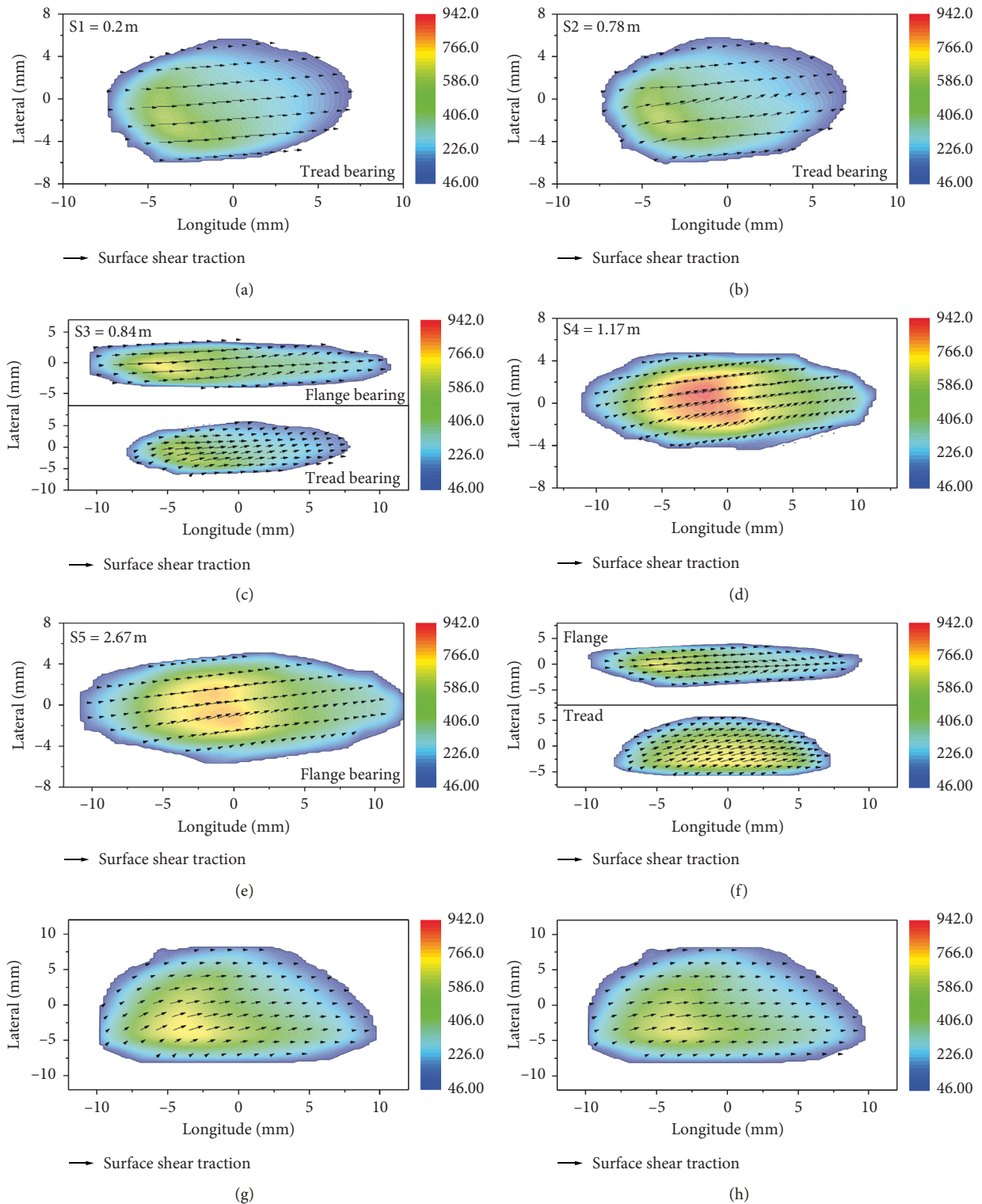


FIGURE 11: The distribution of surface shear stress in the tread bearing part and flange bearing part during transition: (a) S1; (b) S2; (c) S3; (d) S4; (e) S5; (f) S6; (g) S7; (h) S8.

on the mainline rail when the wheel load is transferred from tread to flange, and the deflection angle between the surface shear stress vector and running direction of the wheel will increase due to the structural irregularity. During transition, the contact patch on flange becomes longer and narrower

and its length increases by 42.3%, while its width decreases by about 32.1%. When the flange solely bears the wheel load as shown in Figure 11(d), the deflection angles between the surface shear stress vector and the theoretical running trajectory located at high stress regions increase

significantly, and the maximum surface shear stress occurs in the bearing flangeway.

Figures 11(e)–11(h) show the distribution of adhesion-slip regions in flange bearing part during transition. Similarly, the deflection angles located at high stress regions increase significantly. The length of the contact patch decreases by 23.4% while the width of the contact patch increases by 40.3% from S5 to S7, and the long and narrow contact patches tend to be elliptic. Due to the flange bearing mode and impact effect, the surface shear stress in bearing flangeway and bearing wing rail are relatively large, and the dramatic surface shear stress acting on the surface can cause obvious plastic deformation of the rail, and degradation will develop and accumulate at high stress locations, leading to a quicker rate of wear. Therefore, the region easily subject to degradation not only includes the bearing flangeway where the flange is bearing the wheel load solely but also includes the bearing wing rail where the maximum vertical contact forces occur.

5.3. Distribution Characteristics of Microslip in the Contact Zone. The nonuniform wear in the turnout can be attributed to the combined effects of various factors, including the contact parameters, geometrical profile, material composition, and wheel-rail relative sliding velocity. According to the Zobory wear model, a higher microslip value corresponds to a quicker wear rate of the material [26]. In order to qualitatively describe the nonuniform wear of frog, microslip in contact patches can be regarded as an essential index for evaluating the wear of frog rails. The magnitude and distribution of the microslip field are shown in Figure 12 at eight typical instants for two transition regions.

As shown in Figure 12, the microslip in the adhesion region equals to zero, and the microslip vector lies in the opposite direction of the surface shear stress. Furthermore, the maximum value of microslip is primarily located at the edge of the contact patch. Due to the impact induced by the structural irregularity, the magnitude of microslip increases from S2 to S4, and the impact between wheel and rail with high-frequency will be transmitted in the form of guide waves, and the vibrations will provide quite distinct effects on different local areas of the contact patch, which will in turn lead to local changes in the magnitude and direction of microslip. When the flange is bearing the entire wheel load at the bearing flangeway, the longitudinal axis of the bearing flangeway is relatively parallel to the running direction of the wheel, so the deflection angle will decrease.

Figures 12(e)–12(h) show the distribution of microslip in flange bearing part during transition. The value of the microslip acting on the wheel tread gradually increases, and the deflection angle between the microslip vector and the trajectory will increase as a result of the misalignment between the longitudinal axle of the bearing flangeway and the running direction. The wheel-rail impact will significantly affect the magnitude and direction of the microslip in the contact patch as shown in Figure 12(f); therefore, the wear will develop and accumulate at the locations corresponding to the impact, exacerbating its effects, which in turn will extend and accelerate the development of nonuniform wear

in the flange bearing frog, leading to problems which will threaten the running quality of the train and rail service properties of the flange bearing frog.

According to the summary of wheel-rail contact solutions calculated above, the stress and geometrical size of contact patches during transition is shown as in Table 3.

6. Study on RCF of Flange Bearing Frog Based on Wear Number

In the long time service of the rail, the contact area is subjected to cyclic rolling, resulting in the initiation and the development of fatigue damage cracks of the material (RCF). In order to identify the typical forms of degradation (wear or RCF damage) exhibited on the surface of different parts of flange bearing frogs, RSSB (the Rail Safety and Standards Board of the UK) standards are applied to investigate the relationship between wear and RCF damage.

During the dynamic interaction between wheel and rail in the frog, the ratio of the contact stress to the plastic shake-down limits varies along the longitudinal direction of rail. The probability of RCF damage occurring on the rails depends not only on the value of the ratio but also on the wear rate. Wear can be considered as the source of rail RCF damage and cracks [26]. Certain wear can prevent the initiation and development of rolling contact fatigue cracks, so it is obvious that wear is beneficial for preventing the occurrence of RCF damage to a certain extent. When the wheel passes the turnout in the divergent direction, the dramatic surface shear stress together with normal contact stress, exacerbated by the structural irregularities, will cause the accumulation of plastic deformation. This takes the form of a ratcheting effect on the material surface layer in the contact region. A rail is always subject to fatigue crack initiation and propagation after long-term service, which can result in RCF damage to materials and poor customer comfort.

Turnout rails with severe wear are always liable to suffer from rolling fatigue damage (Figure 13). According to the field experiment data measured in actual condition, the damage coefficients obtained based on wear numbers coincide well with the practical data [27, 28]. The mutual competitive relationship between wear and RCF damage can be calculated based on the wheel-rail wear model and the RCF damage functions. The focus in our paper is to predict the dominant degradation exhibited on surface of different parts in flange bearing frog, so the RSSB (Rail safety and standards board of the UK) based on principle of energy dissipation is applied, considering the coupled competitive relationship between wear and RCF damage. The coupled competitive relationship between wear and surface RCF can be expressed via the equation as described below:

$$P_f = \begin{cases} 1, & T_\gamma \leq 65N, \\ \frac{35}{22} - \frac{T_\gamma}{110}, & 65N < T_\gamma < 175N, \\ 0, & T_\gamma \geq 175N, \end{cases} \quad (3)$$

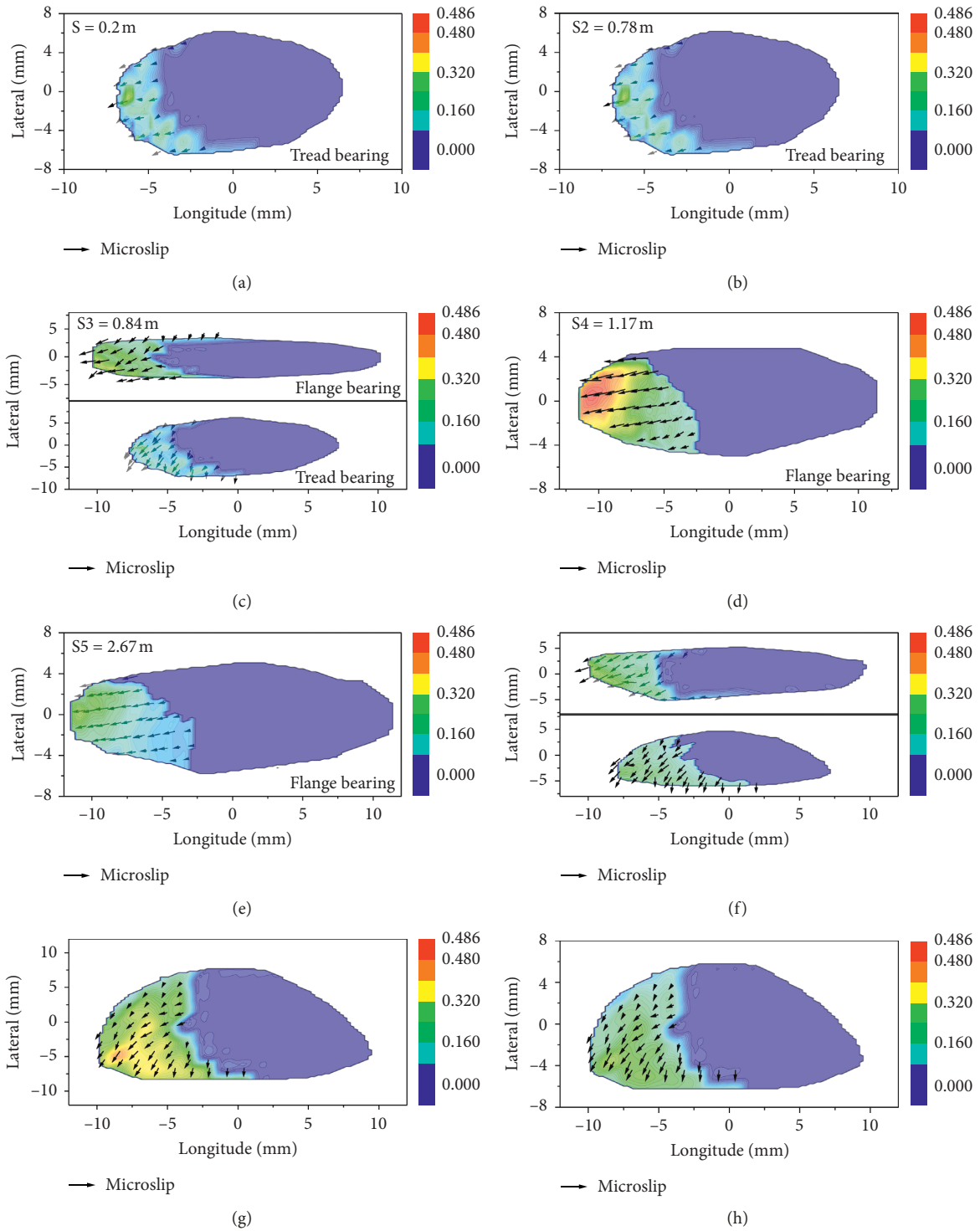


FIGURE 12: The distribution of microslip in the tread bearing part and flange bearing part during transition: (a) S1; (b) S2; (c) S3; (d) S4; (e) S5; (f) S6; (g) S7; (h) S8.

where $T_v = T_x \xi_x \times T_z \xi_z$ is the wear number, which is the principal parameter to determine the dominant damage form on the flange bearing frog rail, and the ξ_x and ξ_z are the creepages along longitudinal and lateral direction; the creepage can be calculated based on the sliding velocity and forward

velocity of the wheel; it can be defined as the ratio between the sliding velocity and the forward velocity.

Figure 14 shows the mutual competition between wear number and RCF damage functions in different contact statuses [29]. The curve of the wheel-rail RCF damage

TABLE 3: The wheel/rail contact information during the transition (15 km/h).

Component	Instant	Contact positions	Contact patch			Max pressure (MPa)	Max surface shear stress (MPa)	Max V-M stress (MPa)
			Longitude (mm)	Lateral (mm)	Area (mm ²)			
Tread bearing part	S2	Tread	8.3	7.6	198.1	1531	606.5	608.2
	S3	Tread	6.5	5.8	118.4	1213	572.8	521.5
	S3	Flange	11.3	3.4	120.7	1843	687.7	1023.4
	S4	Flange	12.1	4.2	159.7	2485	942.0	1397
Flange bearing part	S5	Flange	11.6	4.0	145.8	1958	903.9	876.7
	S6	Flange	9.8	3.7	113.9	1542	689.4	823.0
	S6	Tread	7.6	5.6	133.7	1547	718.1	864.2
	S7	Tread	9.8	8	246.3	2014	818.5	1137

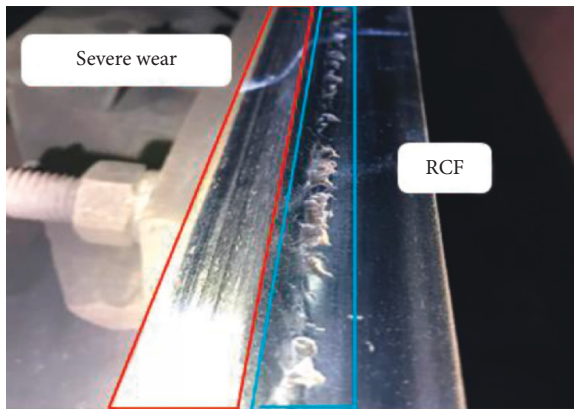


FIGURE 13: Wear and RCF damage to the frog rail.

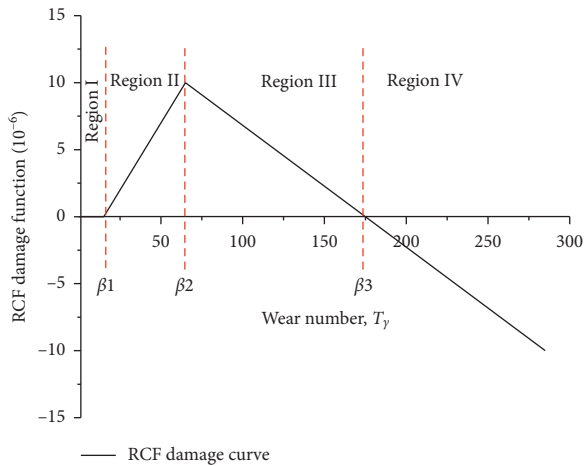


FIGURE 14: RCF damage function based on wear index.

functions can be divided into 4 regions, where the wear and RCF damage occupy the dominant position in different regions, respectively. For region I, the value of RCF damage is 0, indicating that the wheel load is less than the shakedown limit of the rail; in this case, plastic deformation under the high stress field will not accumulate, and this has no effect on promoting the development of RCF in the frog. For region II, the RCF damage will be intensified with the increase of the wear index until the maximum value has been reached. For region III, the wear development velocity gradually

grows faster than that of the RCF damage, in line with the sustained growth of the wear index. RCF damage will gradually decrease to 0 under serious wear conditions. For region IV, materials suffering from RCF damage will be completely lost due to wear; it can therefore be considered that almost no RCF occurs at this time and that the most dominant form of damage in this region is the wear. However, the values of wear rate have different effects on the initiation and propagation of fatigue crack. Under the effect of cyclic loading on frog rail, the wheel-rail plastic strain will accumulate, and the toughness of material will reach its limit, leading to the failure of the material, and the material of rail will suffer from RCF damage or wear at the same time; if the wear rate exceeds the crack propagation rate, the local surface of rail with tiny crack is worn, so the length of crack will decrease or remain constant; however, if the crack propagation rate exceeds the wear rate, the growth of crack will be greater than zero. Under the effect of contact stress, the length of crack will continue to increase when the propagation rate of crack exceeds the wear rate, so the rail will be in the stage of fatigue failure at this time [30].

In order to identify the regions in the flange bearing frog where the wear or the RCF damage occupies the dominant position, the wear index is calculated when the wheel passes through the frog at approximately 15 km/h in the facing divergent direction. Intensified dynamic wheel-rail interaction will be excited due to the inherent structural irregularity of the frog. The wear development rate of the frog rail surface will therefore increase significantly. The maximum value of the wear index is located at the region where the entire load is being carried by the flange; in the flange bearing regions, the wear rate can obviously develop and accumulate under high stress and creep conditions, exacerbating the impact and stress levels, which will in turn extend and accelerate the wear. Therefore, due to the mutual competition between the RCF damage coefficient and the wear index, different degrees of wear correspond to different rates of RCF damage.

As shown in Figures 15 and 16, Region I does not contain any regions. In Region II, the RCF damage rate grows at a relatively faster rate in two-point contact status during transition in tread bearing part. Thus, the RCF damage rate will not keep growing with an increase in wear index; instead, the RCF damage rate will drop in line with the sustained growth of the wear index due to mutual competition

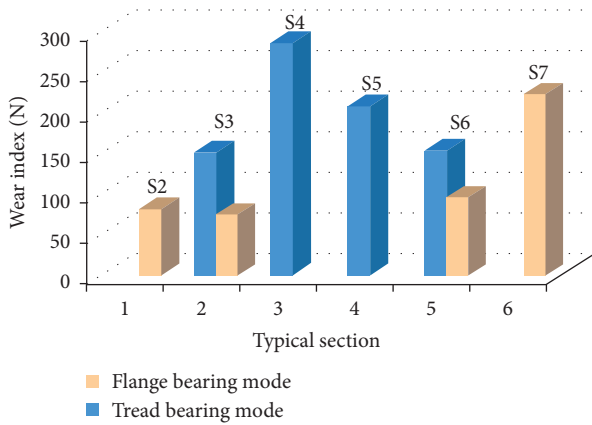


FIGURE 15: Wear index of flange bearing frog.

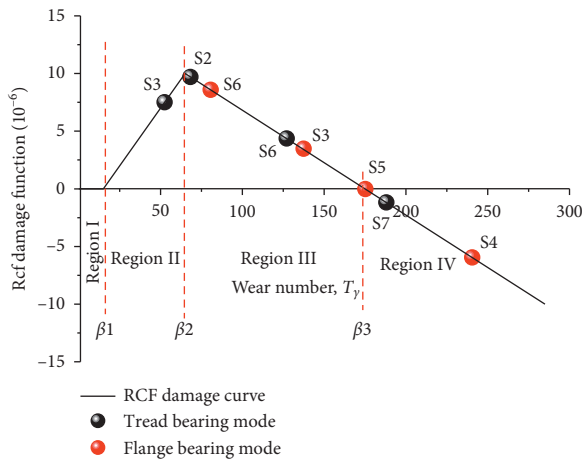


FIGURE 16: RCF damage function of typical sections.

of wear and RCF damage. This will decrease the RCF damage rate due to the higher wear encountered during two-contact state. In Region III, the wear development rate at the mainline rail will gradually exceed the RCF damage development. The transition regions are mainly located at areas in Regions II and III, and the dominant degradation forms in the aforementioned areas may possibly be affected by both the wear and RCF damage during the transition. The bearing flangeway together with the bearing wing rail of the flange bearing part corresponding to a higher contact force value is located in Region IV. The material suffering from RCF damage is worn due to the violent wear exacerbated by the impact and the higher stress field effect, meaning that RCF damage cannot exist or develop on the surface of a rail impacted by violent wear. Wear will be the dominant form of degradation influencing the dynamic performance and service life of the bearing flangeway and bearing wing rail; therefore, the parts of frog rail exhibits RCF should select the material with low strength, low crack initiation, and growth rate, so the RCF damage can be reduced by the wear rate; the parts of frog rail exhibits wear should select the material with higher hardness and yield strength, which can help prevent the development of wear, and the optimization material

composition can decrease the cost of maintenance. In addition, the rail maintenance measures are different under different damage conditions, which depend on the specific damage form; the frog can enhance the safety and efficiency through the method of target maintenance. In addition, according to reference [31], the possibility of RCF damage P_r can be described as follows:

$$P_r = d_r - C_r \times T_\gamma, \quad (4)$$

where d_r is the extent of contact stress exceeding the stability limit and C_r is the wear rate factor obtained through the experiment. As can be seen, the RCF life mainly depends on the extent of contact stress exceeding the stability limit, so in order to compare the expected life of conventional fixed frog and flange bearing frog for this type of service, the comparison of contact stress (Table 1) can be applied to investigate the life of each frog qualitatively. Compared to the contact stress of fixed frog in reference [16], the maximum contact stress of flange bearing frog is no more than two times the conventional fixed frog. However, in this type of service, it is obvious that when the number of diverging passing vehicles is less than 1% of the number of straight passing vehicles, the through direction will be the dominant factor controlling the RCF life, so the RCF life of flange bearing frog is longer than the conventional fixed frog.

7. Conclusion

In this article, the wheel-rail contact behavior together with the distribution characteristics of contact solutions taking into account surface shear stress, microslip, and adhesion slip is analyzed using a 3D explicit finite element model for the period when the wheel passes the frog in a facing divergent direction at 15 km/h. Special attention is paid to the distribution of the wear index during transition. The wear index is then applied to calculate the RCF damage to recognize the dominant form of degradation along the transition region of the flange bearing frog. Conclusions are drawn as follows:

- (1) There are mainly two wheel-load transition regions in the flange bearing frog when the wheel passes the frog. The wheel load is transferred from the tread to the flange and back to the tread in the transition region. The contact force will reach a maximum value of 181 kN due to the height difference between mainline rail and bearing flangeway, and the contact patch tends to be narrower and longer when the flange is solely bearing the entire wheel load.
- (2) The maximum value of microslip is located at the edge of the contact patch and can be intensified by the structural irregularities of frog. Additionally, the area of slip region in the contact patch will significantly increase due to the impact and traction effect. This can lead to violent wear on the surface of the frog with the joint effect of the two factors mentioned above.
- (3) Due to the small size of the contact patches and the significant difference in contact radius, together with

the normal contact force, the surface shear stress field is relatively large when the flange is solely bearing the entire wheel load, which can lead to the development and accumulation of severe wear. Hence, the bearing flangeway tends to be the key component influencing passenger comfort and service life of frog rails.

- (4) The bearing flangeway will be the region suffering from the most severe wear under high stress and creep conditions, and the wear is the dominant damage factor at the bearing flangeway where the flange is bearing the entire wheel load. Both wear and RCF damage have a certain effect on the degradation of the frog in the two-contact state during transition. The RCF damage rate increases at the highest speed at the bearing wing rail of the flange bearing part.

In order to obtain an accurate understanding of the behavior of dynamic wheel-rail interaction and the associated degradation at the flange bearing frog, a long-time field tracking test will be performed to observe both the distribution of bands and the evolution of the profile. The data from the tests will then be analyzed to verify the accuracy of the model, which will be adopted as a theoretical basis for rail structure optimization, damage relief, and maintenance of flange bearing frogs.

Data Availability

The data used to support the findings of this study are available from the corresponding author upon request.

Conflicts of Interest

The authors declare that they have no conflicts of interest.

Acknowledgments

This study was supported by the National Key R&D Program of China (2017YFB1201102), the National Natural Science Foundation of China (51608459, 51778542, and U1734207), Fundamental Research Funds for the Central Universities (2682018CX01), and Cultivation Program for the Excellent Doctoral Dissertation of Southwest Jiaotong University.

References

- [1] P. Wang, X. C. Ma, J. Wang, J. Xu, and R. Chen, "Optimization of rail profiles to improve vehicle running stability in switch panel of high-speed railway turnouts," *Mathematical Problems in Engineering*, vol. 2017, Article ID 2856030, 13 pages, 2017.
- [2] P. Wang, X. Ma, J. Xu, J. Wang, and R. Chen, "Numerical investigation on effect of the relative motion of stock/switch rails on the load transfer distribution along the switch panel in high-speed railway turnout," *Vehicle System Dynamics*, vol. 57, no. 2, pp. 226–246, 2019.
- [3] J. Xu, J. Wang, P. Wang et al., "Study on the derailment behaviour of a railway wheelset with solid axles in a railway turnout," *Vehicle System Dynamics*, vol. 58, no. 1, pp. 123–143, 2020.
- [4] J. Xu, P. Wang, X. Ma, J. Xiao, and R. Chen, "Comparison of calculation methods for wheel-switch rail normal and tangential contact," *Proceedings of the Institution of Mechanical Engineers, Part F: Journal of Rail and Rapid Transit*, vol. 231, no. 2, pp. 148–161, 2016.
- [5] C. Andersson and T. Dahlberg, "Wheel/rail impacts at a railway turnout crossing," *Proceedings of the Institution of Mechanical Engineers, Part F: Journal of Rail and Rapid Transit*, vol. 212, no. 2, pp. 123–134, 1998.
- [6] E. Kassa and J. C. O. Nielsen, "Dynamic train–turnout interaction in an extended frequency range using a detailed model of track dynamics," *Journal of Sound and Vibration*, vol. 320, no. 4–5, pp. 893–914, 2009.
- [7] S. Alfi and S. Bruni, "Mathematical modelling of train–turnout interaction," *Vehicle System Dynamics*, vol. 47, no. 5, pp. 551–574, 2009.
- [8] Z. Ren, S. Sun, and G. Xie, "A method to determine the two-point contact zone and transfer of wheel-rail forces in a turnout," *Vehicle System Dynamics*, vol. 48, no. 10, pp. 1115–1133, 2010.
- [9] A. Johansson, B. Pålsson, M. Ekh et al., "Simulation of wheel-rail contact and damage in switches & crossings," *Wear*, vol. 271, no. 1–2, pp. 472–481, 2011.
- [10] J. M. Rocha, A. A. Henriques, and R. Calçada, "Probabilistic assessment of the train running safety on a short-span high-speed railway bridge," *Structure and Infrastructure Engineering*, vol. 12, no. 1, pp. 78–92, 2016.
- [11] J. M. Rocha, A. A. Henriques, and R. Calçada, "Safety assessment of a short span railway bridge for high-speed traffic using simulation techniques," *Engineering Structures*, vol. 40, pp. 141–154, 2012.
- [12] M. Wiest, W. Daves, F. D. Fischer, and H. Ossberger, "Deformation and damage of a crossing nose due to wheel passages," *Wear*, vol. 265, no. 9–10, pp. 1431–1438, 2008.
- [13] F. Greco, P. Lonetti, and A. Pascuzzo, "A moving mesh FE methodology for vehicle–bridge interaction modeling," *Mechanics of Advanced Materials and Structures*, pp. 1–13, 2018.
- [14] P. Lonetti, A. Pascuzzo, and A. Davanzo, "Dynamic behavior of tied-arch bridges under the action of moving loads," *Mathematical Problems in Engineering*, vol. 2016, Article ID 2749720, 17 pages, 2016.
- [15] D. D. Davis, J. Lopresti, and S. Kalay, "Improved performance track components for heavy axle loads and high speed rail," in *Proceedings of the Joint Rail Conference*, Pueblo, CO, USA, March 2011.
- [16] M. Pletz, W. Daves, and H. Ossberger, "A wheel set/crossing model regarding impact, sliding and deformation-explicit finite element approach," *Wear*, vol. 294–295, pp. 446–456, 2012.
- [17] M. Pletz, W. Daves, and H. Ossberger, "A wheel passing a crossing nose: dynamic analysis under high axle loads using finite element modelling," *Proceedings of the Institution of Mechanical Engineers, Part F: Journal of Rail and Rapid Transit*, vol. 226, no. 6, pp. 603–611, 2012.
- [18] S. L. Guo, D. Y. Sun, F. C. Zhang, X. Y. Feng, and L. H. Qian, "Damage of a Hadfield steel crossing due to wheel rolling impact passages," *Wear*, vol. 305, no. 1–2, pp. 267–273, 2013.
- [19] L. Xin, V. L. Markine, and I. Y. Shevtsov, "Numerical procedure for fatigue life prediction for railway turnout crossings using explicit finite element approach," *Wear*, vol. 366–367, pp. 167–179, 2016.
- [20] Z. L. Wei, C. Shen, Z. L. Li, and R. Dollevoet, "Wheel–rail impact at crossings: relating dynamic frictional contact to

- degradation,” *Journal of Computational and Nonlinear Dynamics*, vol. 12, no. 4, Article ID 041016, 2017.
- [21] Z. Wei, A. Núñez, A. Boogaard, R. Dollevoet, and Z. Li, “Method for evaluating the performance of railway crossing rails after long-term service,” *Tribology International*, vol. 123, pp. 337–348, 2018.
- [22] Y. Ma, A. A. Mashal, and V. L. Markine, “Modelling and experimental validation of dynamic impact in 1:9 railway crossing panel,” *Tribology International*, vol. 118, pp. 208–226, 2018.
- [23] W. Zhao, D. Song, and B. Liu, “Error bounds and finite termination for constrained optimization problems,” *Mathematical Problems in Engineering*, vol. 2014, Article ID 158780, 10 pages, 2014.
- [24] W. M. Zhai, *Vehicle-Track Coupling Dynamics*, Science Press, Beijing, China, 3rd edition, 2017.
- [25] X. Zhao, X. Zhao, C. Liu, Z. Wen, and X. Jin, “A study on dynamic stress intensity factors of rail cracks at high speeds by a 3D explicit finite element model of rolling contact,” *Wear*, vol. 366-367, pp. 60–70, 2016.
- [26] I. Z. I. Zobory, “Prediction of wheel/rail profile wear,” *Vehicle System Dynamic*, vol. 28, no. 2-3, pp. 221–259, 1997.
- [27] D. Babette and E. Roger, “Prediction model for wheel profile wear and rolling contact fatigue,” *Wear*, vol. 271, no. 1-2, pp. 210–217, 2011.
- [28] J. Brouzoulis, P. T. Torstensson, and R. Stock, “Prediction of wear and plastic flow in rails-test rig results, model calibration and numerical prediction,” *Wear*, vol. 271, no. 1-2, pp. 92–99, 2011.
- [29] A. Bevan, P. Molyneux-Berry, B. Eickhoff, and M. Burstow, “Development and validation of a wheel wear and rolling contact fatigue damage model,” *Wear*, vol. 307, no. 1-2, pp. 100–111, 2013.
- [30] M. C. Burstow, *Whole Life Rail Model Application and Development for RSSB-Continued Development of an RCF Damage Parameter*, Rail Standards and Safety Board, London, UK, 2004.
- [31] W. R. Tyfour, J. H. Beynon, and A. Kapoor, “Deterioration of rolling contact fatigue life of pearlitic rail steel due to dry-wet rolling-sliding line contact,” *Wear*, vol. 197, no. 1-2, pp. 255–265, 1996.



Hindawi

Submit your manuscripts at
www.hindawi.com

